energies

MDPI

Article

Design of Parallel Air-Cooled Battery Thermal Management System through Numerical Study

Kai Chen [1,*], Zeyu Li [1], Yiming Chen [1], Shuming Long [1], Junsheng Hou [1], Mengxuan Song [2] and Shuangfeng Wang [1,*]

[1] Key Laboratory of Enhanced Heat Transfer and Energy Conservation of the Ministry of Education, School of Chemistry and Chemical Engineering, South China University of Technology, Guangzhou 510640, China; dedicatedlzy@126.com (Z.L.); cym665566@163.com (Y.C.); smlongs@163.com (S.L.); hjs_scut@163.com (J.H.)

[2] Department of Control Science and Engineering, Tongji University, Shanghai 201804, China; songmx@tongji.edu.cn

* Correspondence: chenkaihb09@126.com (K.C.); sfwang@scut.edu.cn (S.W.); Tel.: +86-020-22236929 (S.W.)

Received: 10 August 2017; Accepted: 19 October 2017; Published: 23 October 2017

Abstract: In electric vehicles, the battery pack is one of the most important components that strongly influence the system performance. The battery thermal management system (BTMS) is critical to remove the heat generated by the battery pack, which guarantees the appropriate working temperature for the battery pack. Air cooling is one of the most commonly-used solutions among various battery thermal management technologies. In this paper, the cooling performance of the parallel air-cooled BTMS is improved through choosing appropriate system parameters. The flow field and the temperature field of the system are calculated using the computational fluid dynamics method. Typical numerical cases are introduced to study the influences of the operation parameters and the structure parameters on the performance of the BTMS. The operation parameters include the discharge rate of the battery pack, the inlet air temperature and the inlet airflow rate. The structure parameters include the cell spacing and the angles of the divergence plenum and the convergence plenum. The results show that the temperature rise and the temperature difference of the batter pack are not affected by the inlet air flow temperature and are increased as the discharge rate increases. Increasing the inlet airflow rate can reduce the maximum temperature, but meanwhile significantly increase the power consumption for driving the airflow. Adopting smaller cell spacing can reduce the temperature and the temperature difference of the battery pack, but it consumes much more power. Designing the angles of the divergence plenum and the convergence plenum is an effective way to improve the performance of the BTMS without occupying more system volume. An optimization strategy is used to obtain the optimal values of the plenum angles. For the numerical cases with fixed power consumption, the maximum temperature and the maximum temperature difference at the end of the five-current discharge process for the optimized BTMS are respectively reduced by 2.1 K and 4.3 K, compared to the original system.

Keywords: battery thermal management; air cooling; system parameters; plenum angle; numerical study

1. Introduction

In recent years, electric vehicles (EVs) and hybrid electric vehicles (HEVs) have attracted worldwide attention due to their cleanness. The lithium battery pack is one of the most important components, which provides the power for EVs and HEVs. Much research has shown that the lithium battery cell performs well at the temperatures ranging between 0 °C and 40 °C and at a temperature difference below 5 °C [1,2]. However, a large amount of heat is generated when the lithium battery is

working. If the heat cannot be removed quickly, the temperature and the temperature difference of the battery pack will increase, finally making the performance worse and shortening the service life of the battery pack. Therefore, the battery thermal management system (BTMS) is critical to dissipate the heat, which can guarantee that the battery pack works within the appropriate temperature range.

Many battery thermal management technologies have been developed in previous studies, including air cooling [3–5], liquid cooling [6–8] and phase change material cooling [9–12]. Compared to other cooling methods, air cooling requires less cost, and the relevant system has a simple structure. Thus, air cooling has become one of the most commonly-used solutions in battery thermal management.

In air-cooled BTMS, the air is the cooling medium and removes the heat generated by the battery cell. The cooling performance is strongly influenced by the airflow pattern in the system, while the flow pattern is determined by the parameters of the BTMS. Efforts have been made to investigate the influences of the parameters on the performance of the BTMS. The status of the inlet air is one of the most important factors that strongly influence the cooling performance of the BTMS, which contains the inlet air temperature and the inlet airflow rate. Yi et al. [13] developed a modeling procedure to study the effects of operating conditions on the thermal performance of a battery module. Various inlet airflow rates and various discharge rates were considered and compared. In the study of Cho et al. [14], the results showed that as the inlet air temperature increased, the maximum temperature of the battery pack was increased and the maximum temperature difference was reduced due to less heat generation of the battery pack. Fan et al. [15] found that the maximum temperature and the maximum temperature difference of the battery pack were both reduced as the inlet flow rate was increased. The increase of the flow rate increased the flow rate in the cooling channels, leading to a large convective heat transfer coefficient. Thus, the cooling performance of the system was improved. However, the study of Liu et al. [16] showed that when the inlet airflow rate was increased for a certain value, the influence of the further increase of the flow rate on the cooling performance will be weakened. He et al. [17] also found that the increase of the inlet velocity reduces the field synergy number, which led to a reduction in the air utilization efficiency.

The structure of the BTMS is another important factor that influences the velocity distribution and temperature distribution of the system. Pesaran et al. [18] compared the performances of the BTMSs with serial ventilation cooling and parallel ventilation cooling. The result showed that the maximum temperature of the battery pack for the parallel ventilation cooling was reduced by 4 °C, and the temperature difference was reduced by 10 °C compared to the serial ventilation cooling. Mahamud et al. [19] adopted the two-dimensional computational fluid dynamics (CFD) model to study the performance of the BTMS with the reciprocating airflow. The numerical result showed that the reciprocating flow can reduce the temperature difference of the battery system by about 4% and the maximum cell temperature by 1.5% for a reciprocation period of 120 s when compared to the unidirectional flow situation. Wang et al. [20] used the CFD method to explore the influence of the battery cell arrangement structure on the thermal performance of the battery module. The numerical result indicated that the performance was better with the axisymmetric battery module structure. Further study showed that the fans that drove the cooling air were suggested to be placed on the top of the module. Yong et al. [21] investigated the influence of the cell spacing on the performance of the lithium-ion battery system, finding that the cell temperature increased as the cell spacing increased when fixing the airflow rate. Park et al. [22] maintained the arrangement of the existing battery pack and improved the cooling performance of the BTMS by adopting the tapered manifold and pressure relief ventilation. Sun et al. [23] also improved the performance of the parallel air-cooled BTMS with Z-type flow through using the tapered inlet and outlet ducts. The maximum lumped cell temperature difference of the battery pack was reduced by 7.2 °C, and the maximum lumped peak cell temperature was reduced by 6.3 °C. Chen et al. [24] introduced the flow resistance network model to calculate the velocities in the cooling channels of the parallel air-cooled BTMS. Then, the model was combined with the Newton method to optimize the angles of the divergence plenum and the convergence plenum for cooling performance improvement. The results showed that the maximum temperature difference of

the battery pack was reduced by 30% or more after optimization. Shahid et al. [25] introduced inlet plenum, multiple vortex generators and jet inlets into the BTMS to remarkably reduce the maximum temperature and the maximum temperature difference of the battery pack.

Previous studies have shown that the CFD method is an effective method to evaluate the performance of the BTMS [26–29]. Many scholars have explored the influences of the parameters of the BTMS on the cooling performance of the system. However, the existing research rarely compares the influences of different parameters on the cooling performances and also rarely gives a suggestion for the optimal parameters. In this paper, the influences of different parameters on the performance of the parallel air-cooled BTMS are investigated and compared. The performance of the system is evaluated through CFD calculation. Typical numerical cases are employed to investigate the influences of the operation parameters and the structure parameters on the temperature and the temperature difference of the battery pack. The main parameters hat influence the performance most are found. Finally, an optimization strategy is used to optimize the main parameters without increasing the total volume and the power consumption of the system, obtaining the optimal parameters of the BTMS for performance improvement.

The remainder of the paper is organized as follows. Section 1 introduces the models to calculate the flow field and temperature field of the parallel air-cooled BTMS. Section 2 introduces the numerical procedure of the test cases. Section 3 studies the influences of the operation parameters and structure parameters on the cooling performance of the system, then the optimal parameters of the system are obtained using an optimization strategy. Section 4 presents the conclusions.

2. Models

2.1. Illustration of the Parallel Air-Cooled BTMS

In the present study, the battery pack with $N \times M$ prismatic battery cells is considered, which is included in the parallel air-cooled BTMS. The schematics of the battery cell and the battery pack are shown as Figure 1. The schematic of the three-dimensional system is depicted in Figure 2a, and the relevant side view of the system is shown in Figure 2b. The cooling air is pumped into the system from the inlet on the left-hand side. In the inlet duct, the air is distributed into the cooling channels, and the heat generated by the battery cells is removed. Then, the air in each cooling channel is converged into the outlet duct and leaves the system from the outlet. For the battery pack, the maximum temperature (T_{max}) and the maximum temperature difference (ΔT_{max}) are two important indices, which are used to evaluate the cooling performance of the BTMS. When designing the system, it is desirable to minimize these two indices. As the cross-sectional areas of the cooling channels are identical, it is easy to know that T_{max} and ΔT_{max} can be reduced through homogenizing the airflow rates in the cooling channels.

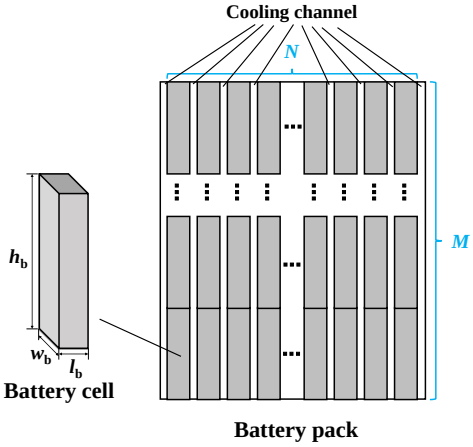

Figure 1. Schematic of the battery pack.

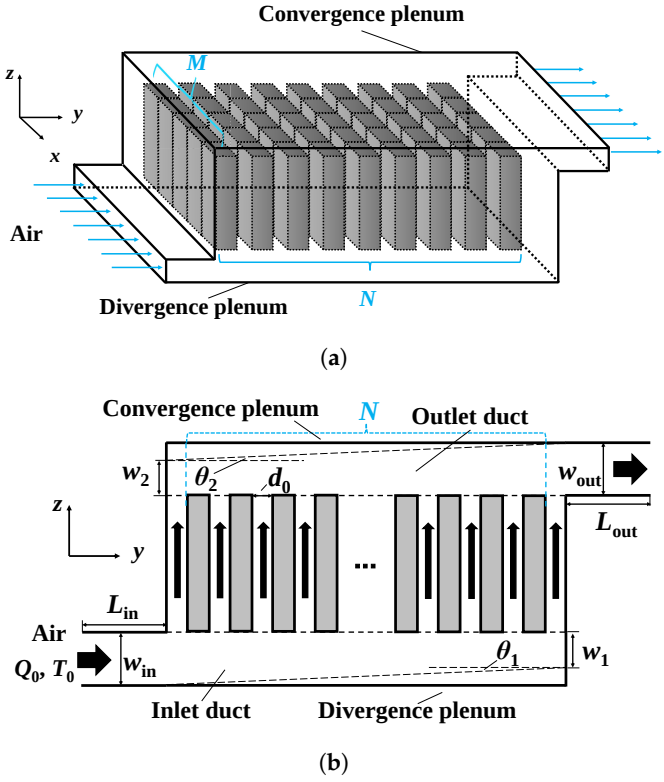

Figure 2. Schematic of the parallel air-cooled battery thermal management system (BTMS). (**a**) Orthographic view of the BTMS; (**b**) Side view of the BTMS.

2.2. Computational Fluid Dynamics Calculation

In order to evaluate the cooling performance of the parallel air-cooled BTMS, the flow field and the temperature field should be obtained. In the present study, the computational fluid dynamics (CFD) method is introduced for velocity calculation and temperature calculation. The solid domain is the area of the battery cells, and the airflow domain is the area of the BTMS except the battery cells, including the inlet duct, the outlet duct and the cooling channels, shown in Figure 2. The governing equation for the airflow is the Navier–Stokes (N-S) equations. The typical orders of the air density, the air dynamic viscosity, the inlet velocity and the inlet width of the system are respectively 1.29 kg/m^3, 1.86×10^{-6} $kg/(m \cdot s)$, 5 m/s and 0.01 m, so the typical Reynolds number of the inlet air velocity is larger than 3000. The status of the air flow in the system is usually turbulence flow. Thus, the Reynolds-averaged N-S equations with the *k*-*ε* turbulence model and without the buoyancy term are employed to calculate the turbulence flow. The governing equations for the airflow are expressed as follows.

Continuity equation:

$$\frac{\partial u_i}{\partial x_i} = 0 \tag{1}$$

Momentum equation:

$$\rho u_j \frac{\partial u_i}{\partial x_j} = -\frac{\partial p}{\partial x_i} + \frac{\partial}{\partial x_j}\left[(\mu + \mu_t)\frac{\partial u_i}{\partial x_j}\right] \tag{2}$$

Turbulent kinetic energy (*k*) equation:

$$\rho u_j \frac{\partial k}{\partial x_j} = \frac{\partial}{\partial x_j}\left[\left(\mu + \frac{\mu_t}{\sigma_k}\right)\frac{\partial k}{\partial x_j}\right] + \frac{\mu_t}{2}\left(\frac{\partial u_i}{\partial x_j} + \frac{\partial u_j}{\partial x_i}\right)^2 - \rho\varepsilon \tag{3}$$

Turbulent kinetic energy dissipation (ε) equation:

$$\rho u_j \frac{\partial \varepsilon}{\partial x_j} = \frac{\partial}{\partial x_j}\left[\left(\mu + \frac{\mu_t}{\sigma_\varepsilon}\right)\frac{\partial \varepsilon}{\partial x_j}\right] + C_1 \frac{\mu_t}{2}\left(\frac{\partial u_i}{\partial x_j} + \frac{\partial u_j}{\partial x_i}\right)^2 \frac{\varepsilon}{k} - C_2 \rho \frac{\varepsilon^2}{k} \tag{4}$$

The expression of μ_t:

$$\mu_t = \rho C_\mu \frac{k^2}{\varepsilon} \tag{5}$$

where u_i and u_j are the Reynolds-averaged velocity components. p is the Reynolds-averaged pressure. ρ is the density of the air. k and ε are the turbulent kinetic energy and the dissipation rate of the turbulent kinetic energy, respectively. μ and μ_t are the molecular dynamic viscosity coefficient and the turbulent dynamic viscosity coefficient, respectively. C_μ, σ_k and σ_ε are the parameters of the k-ε turbulence model.

The heat generated by the battery cell depends on the cell temperature, the discharge rate and the state of the charge (SOC). Therefore, the heat generation rate changes with time. Therefore, the unsteady temperature equations are introduced to calculate the temperature fields of the air and the battery pack, shown as follows.

Temperature equation for airflow:

$$c_{p,\mathrm{air}} \frac{\partial T_{\mathrm{air}}}{\partial t} + \rho c_{p,\mathrm{air}} u_j \frac{\partial T_{\mathrm{air}}}{\partial x_j} = \frac{\partial}{\partial x_j}\left[\left(\lambda_{\mathrm{air}} + \frac{\mu_t}{\sigma_T}\right)\frac{\partial T_{\mathrm{air}}}{\partial x_j}\right] \tag{6}$$

Temperature equation for the battery pack:

$$\rho_b c_{p,b} \frac{\partial T_b}{\partial t} = \frac{\partial}{\partial x_j}\left[\left(\lambda_b \frac{\partial T_b}{\partial x_j}\right)\right] + \phi_b \tag{7}$$

where T_{air} and T_b are the temperatures of the air and the battery cell, respectively. λ_{air} and λ_b are the thermal conductivity of the air and the battery cell, respectively. $c_{p,\mathrm{air}}$ and $c_{p,b}$ are the heat capacities of the air and the battery, respectively. ρ_b is the density of the battery cell. ϕ_b is the heat generation rate of the battery cell. σ_T are the parameters of the k-ε turbulence model. Typical values of the parameters are shown as below.

$$C_\mu = 0.09, C_1 = 1.44, C_2 = 1.92, \sigma_k = 1.0, \sigma_\varepsilon = 1.3, \sigma_T = 0.85 \tag{8}$$

Besides the governing equations, boundary conditions are essential for velocity calculation and temperature calculation. The mass flow inlet is set as the inlet condition, and the pressure outlet is set as the outlet condition. On the surrounding wall, non-slip conditions and the adiabatic conditions are imposed. On the interface of the air and the battery cells, the temperature continuity and heat flux continuity conditions are imposed. The boundary conditions for the governing equations are expressed as:

$$\begin{aligned}
&\text{Inlet :} \quad u_x = u_z = 0, u_y = u_0, T_{\mathrm{air}} = T_0 \\
&\text{Surrounding wall :} \quad u_x = u_y = u_z = 0, \tfrac{\partial T_{\mathrm{air}}}{\partial \vec{n}} = 0, \\
&\text{Interface wall :} \quad u_x = u_y = u_z = 0, (\lambda_{\mathrm{air}} + \mu_t/\sigma_T)\tfrac{\partial T_{\mathrm{air}}}{\partial \vec{n}} = \lambda_b \tfrac{\partial T_b}{\partial \vec{n}}.
\end{aligned} \tag{9}$$

The software GAMBIT is used to mesh the calculation domain. As the domain is cuboid, the three-dimensional cuboid structural grid system is introduced to discretize the domain. The grids near the walls are refined, and the size of the first layer grids is less than 0.1 mm. The enhanced wall function is used to calculate the velocity distribution inside the boundary layer. The solver type is chosen as the pressure-based type. The governing equations and the boundary conditions are discretized by the finite volume method. The diffusive terms and the convective terms of the equations

are discretized by central-differencing scheme and the second-order upwind scheme, respectively. The discretized equations are solved using the SIMPLE (Semi-Implicit Method for Pressure Linked Equation) algorithm. Finally, the governing equations are solved using the software FLUENT.

3. Numerical Procedure

3.1. Parameters of the Numerical Cases

The parallel air-cooled BTMS shown as Figure 2 is investigated using the CFD method in the present study. The battery pack with 12 × 2 prismatic battery cells is included in the system. The battery cell in the study of Park [22] is introduced. The detailed properties of the cell and the air are summarized in Table 1. The inlet width (w_{in}) and the outlet width (w_{out}) of the system are both set as 20 mm. The cell spacings among the battery cells (the widths of the cooling channels) are 3 mm. The inlet region and the outlet region are enlarged to reduce their influences on the calculation results. The lengths of these two regions (L_{in} and L_{out}) are set as 100 mm. The inlet airflow rate is set as 0.012 m^3/s, with the air temperature at 300 K. The Reynolds number relative to the inlet air velocity is $Re = \rho u d/\mu = 2\rho Q_0/\mu(2w_b + w_{in}) = 10{,}022$. Thus, the air flow in the system is turbulence flow. The unsteady heat generation model developed by experiment for a 2.2-Ah $LiPePO_4$ is used to calculate the heat generation rate of the battery, shown as [16].

$$\phi_b = I^2 R / V_{cell} \tag{10}$$

$$R = 27.54 - 27.68 \times \exp\left(-1.91/T_{cell}\right) + \frac{223.71}{1+21.61\times SOC} - 225.06 \times \frac{\exp(-1.91/T_{cell})}{1+21.61\times SOC} \tag{11}$$

where I is the discharge current. R and V_{cell} are the equivalent resistance and the volume of the battery cell, respectively. T_{cell} is the battery cell temperature. In the present study, a high current discharge rate is considered, so the heat generation rate expressed in Equation (10) only contains the Joule heat. The discharge process with the five-current (5C) constant discharge rate from 95% SOC to 5% SOC is considered. The one-current (1C) discharge process represents that the battery cell with full capacity finishes the discharge in 1 h. The n-current (nC) discharge process represents that the battery cell with full capacity finishes the discharge in $1/n$ h. When the residuals of the discretized equations all fall below 10^{-6}, the simulation is stopped, and the final numerical result is obtained.

Table 1. Properties of the battery cell and air.

Property	Air	Battery Cell [22]
Density (kg/m^3)	1.165	2700
Specific heat ($J/(kg \cdot K)$)	1005	900
Dynamic viscosity ($kg/(m \cdot s)$)	1.86×10^{-5}	-
Thermal conductivity ($W/(m \cdot K)$)	0.0267	240
Initial temperature (K)	300	300
l_b (mm)	-	16
h_b (mm)	-	151
w_b (mm)	-	65

3.2. Grid Dependence Analysis

Before analyzing the calculation result, grid dependence analysis is conducted to determine the appropriate grid size for the CFD calculation. As the calculation domain and the boundary conditions are both symmetric with the plane at $x = 0$, half of the domain is considered as the calculation domain. Various grid sizes are used to discretize the domain, and the maximum temperatures of the battery pack (T_{max}) at the end of the 5C discharge process for various grid sizes are shown in Figure 3. It can be seen that the values of T_{max} do not change when the number of the grids is larger than 2.3×10^6. Finally, the schematic of the grid system at a certain x cross-section is depicted in Figure 4. Moreover,

the maximum $y+$ value of the wall is 1.0, which meets the demand of the enhanced wall function ($y+\leq 1$). Therefore, the grid number of 2.3×10^6 is the appropriate grid number for calculation domain discretization, and a similar grid size is adopted for the following numerical cases.

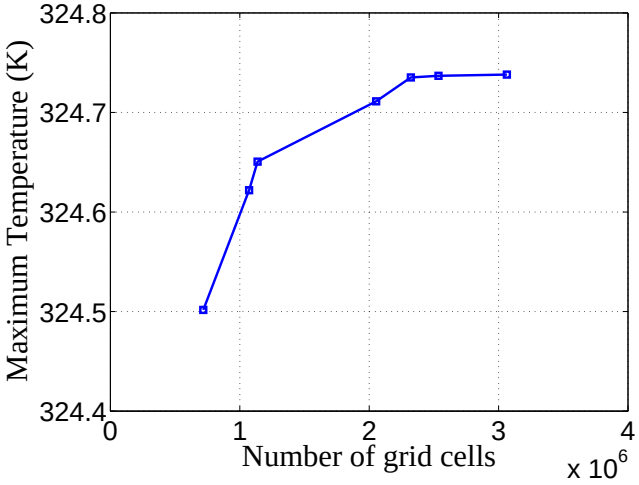

Figure 3. Grid dependence analysis result.

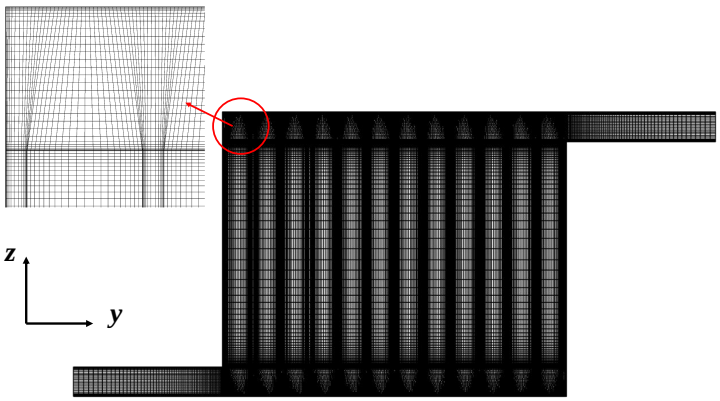

Figure 4. Schematic of the grid system at a certain x cross-section.

As the length of the BTMS along the x-axis is large, the two-dimensional (2D) calculation is performed to approximate the three-dimensional (3D) CFD calculation. The calculation domain of the 2D calculation is shown in Figure 2b. Figure 5 shows the comparison of the maximum temperature (T_{max}) and the maximum temperature difference (ΔT_{max}) of the battery pack with time for the 2D calculation and 3D calculation. It can be observed that the results of the 2D calculation agree well with the ones of the 3D calculation. The average relative errors of T_{max} and T_{min} during the 5C discharge process between the two calculations are both only 0.03 K, respectively. Table 2 lists the comparison of T_{max} and ΔT_{max} at the end of the 5C discharge process for various inlet airflow rates. The errors of T_{max} and ΔT_{max} for different situations are no more than 0.2 K. Furthermore, the 2D calculation needs much less calculation time to obtain the numerical result than the 3D one. Therefore, the 2D calculation is used to evaluate the cooling performance of the BTMS for the following study.

Table 2. Comparison of numerical results at the end of the five-current (5C) discharge process by 2D calculation and 3D calculation.

Q_0	3D Calculation		2D Calculation	
(m^3/s)	T_{max} (K)	ΔT_{max} (K)	T_{max} (K)	ΔT_{max} (K)
0.005	329.5	4.4	329.5	4.4
0.010	327.1	6.6	327.2	6.6
0.012	326.4	7.2	326.5	7.3
0.015	325.4	8.0	325.6	8.2

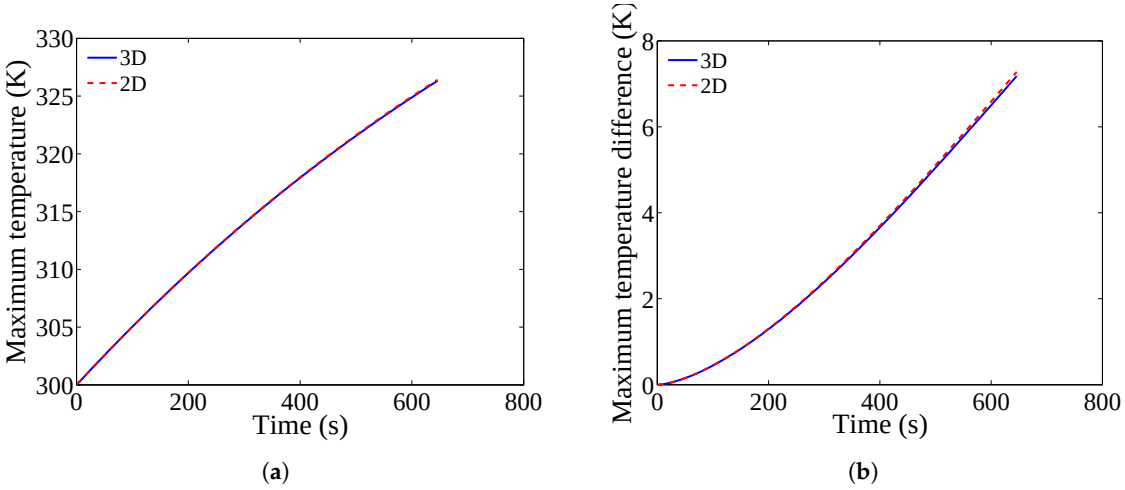

Figure 5. Comparison of the numerical results by 2D calculation and 3D calculation. (**a**) Maximum temperature; (**b**) maximum temperature difference.

3.3. Validation of the CFD Method

A previous study [30] has compared the velocity calculation by the present CFD method with the one in Park's study [22]. The results showed that the average error between them was only 2%, which validated the effectiveness of the present CFD method for velocity calculation. In order to test the effectiveness of the CFD method for temperature calculation, the numerical result of the present method is compared to the experimental data in the reference. In Wu's study [31], the 5C discharge process for the battery cell was tested, and the temperature of the cell was measured. The experimental data are used to validate the result of the present CFD method. The prismatic battery cell with the size of 70 mm × 27 mm × 90 mm used in Wu's study is introduced. The relevant properties of the battery cell are listed in Table 3. The cell is surrounded with air with the temperature at 304.15 K, and the relative convective heat transfer coefficient is 5 $W/(m^2 \cdot K)$. Figure 6 shows the comparison of surface temperature of the battery cell with time by the present CFD method and by the experiment in Wu's study [31]. It can be observed that the numerical result in the present study agrees well with the experimental data. The average error and the maximum error between the two results are respectively 0.7 K and 1.3 K, validating the effectiveness of the present CFD method for temperature calculation.

Table 3. Properties of battery cell used for testing the temperature calculation [31].

Property	Value [31]
Size (mm × mm × mm)	70 × 27 × 90
Density (kg/m^3)	2335
Specific heat ($J/(kg \cdot K)$)	935
Thermal conductivity ($\lambda_x, \lambda_y, \lambda_z$, $W/(m \cdot K)$)	0.26/0.7/0.26
Equivalent heat generation rate (W/m^3)	1.27×10^5

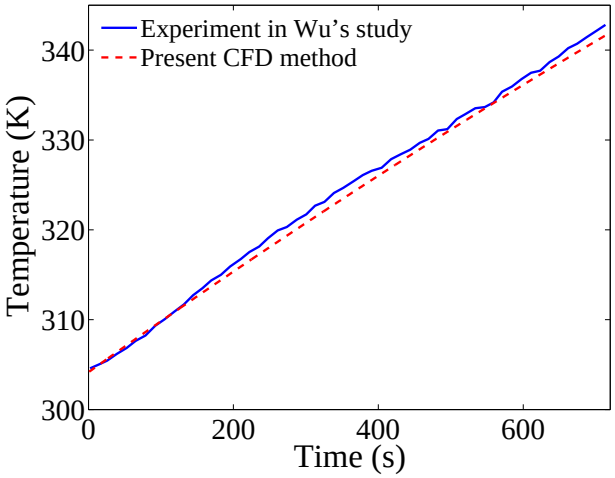

Figure 6. Comparison of the numerical results of the present study and the experiment data in the reference.

4. Influences of the System Parameters on Performance

For the parallel air-cooled BTMS, the values of T_{max} and ΔT_{max} strongly depend on the operation parameters and the structure parameters of the system. The operation parameters include the discharge rate, the inlet air temperature (T_0) and the inlet airflow rate (Q_0). The structure parameters include the cell spacing (d_0) and the angles of the divergence plenum and convergence plenum (θ_1 and θ_2). In the following content, the influences of these parameters on the cooling performance of the BTMS are explored using the CFD method. Finally, an optimization strategy is introduced to obtain the optimal parameters.

4.1. Influence of the Discharge Rate

The heat generation rate of the battery cell depends on the discharge rate. This section considers various discharge rates as 3-current (3C), 4-current (4C), 5-current (5C) and 6-current (6C) and conducts the CFD calculation respectively. The comparison of the numerical results is shown in Table 4. It can be observed that T_{max} and ΔT_{max} both increase as the discharge rate increases. In the BTMS, the temperature difference of the air is not large, so the properties of the air can be treated to be independent of temperature. That means the temperature calculation is decoupled from the velocity calculation. Therefore, the change of discharge rate does not affect the flow field in the BTMS. When the discharge rate increases, the discharge current increases and the heat generation rate increases, which will increase the temperature and the temperature difference of the battery pack. Therefore, reducing the discharge rate can help to reduce T_{max} and ΔT_{max} of the battery pack. In reality, when the EV starts or accelerates, more power is needed from the battery pack, and the discharge rate is larger. In these situations, the temperature rise and the temperature difference of the battery pack are large, and thermal runaway is likely to be induced. However, the power consumption of the battery pack usually depends on the properties of the battery cell and the actual power requirement of the EV. The discharge rate cannot be controlled effectively. Therefore, reducing the discharge rate is not a realizable way to reduce the temperature of the battery pack.

Table 4. Numerical results for various discharge rates of the battery pack.

Discharge Rate	T_{max} (K)	T_{min} (K)	ΔT_{max} (K)
3C	313.5	308.5	5.0
4C	320.0	313.7	6.3
5C	326.5	319.2	7.3
6C	333.5	325.1	8.4

4.2. Influence of the Inlet Air Temperature

Consider various situations of the inlet air temperature (T_0) as 290 K, 295 K, 300 K, 305 K and 310 K and respectively conduct the CFD calculation. The comparison of the numerical results is shown in Figure 7, and the values of T_{max}, ($T_{max} - T_0$) and ΔT_{max} at the end of the 5C discharge process are shown in Table 5. It can be observed that the maximum temperature rise ($T_{max} - T_0$) and the maximum temperature difference ΔT_{max} are independent of T_0. Note that T_0 does not affect the flow field in the BTMS. When T_0 is increased or decreased by a certain value, the whole temperature field is increased or decreased by the same value. In reality, the inlet air temperature can be reduced through refrigeration equipment, such as the air conditioner. However, reducing the inlet air temperature can only reduce the absolute temperature, but cannot reduce the temperature difference of the battery pack. Moreover, the introduction of the refrigeration equipment will require additional power consumption. Therefore, it can be concluded that reducing the inlet air temperature is not an effective way to reduce the temperature difference of the battery pack.

Table 5. Numerical results for various inlet air temperatures.

T_0 (K)	T_{max} (K)	($T_{max} - T_0$) (K)	ΔT_{max} (K)
290	316.5	26.5	7.3
295	321.5	26.5	7.3
300	326.5	26.5	7.3
305	331.5	26.5	7.3
310	336.5	26.5	7.3

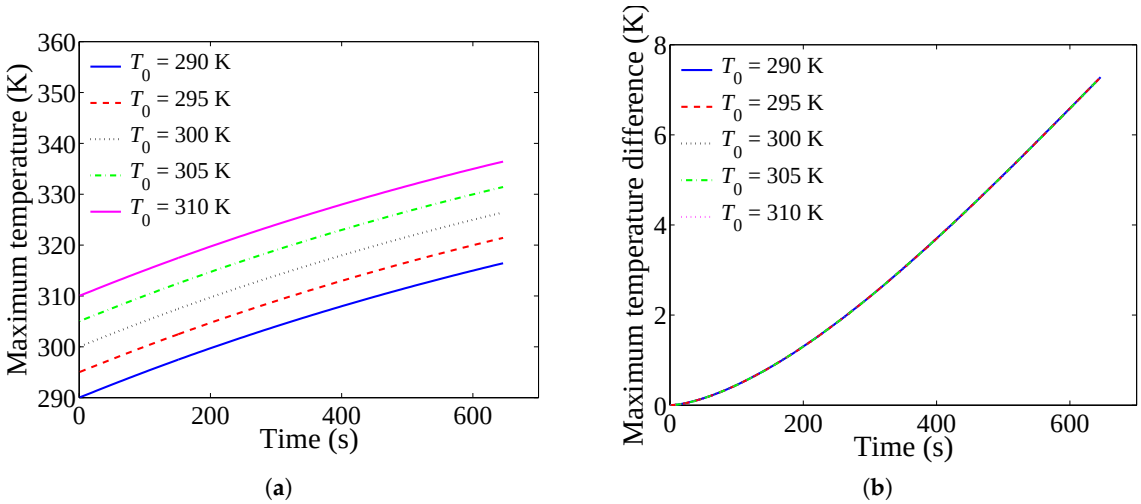

(**a**) (**b**)

Figure 7. Comparison of numerical results for various inlet air temperatures. (**a**) Maximum temperature; (**b**) maximum temperature difference.

4.3. Influence of the Inlet Airflow Rate

Consider various situations of the inlet airflow rates (Q_0) as 0.005 m^3/s, 0.010 m^3/s, 0.012 m^3/s, 0.015 m^3/s and 0.020 m^3/s, and conduct the CFD calculation respectively. Figure 8 depicts the comparison of the airflow rates in the cooling channels and the values of T_{max} and ΔT_{max} with time for various values of Q_0. Table 6 summarizes the results at the end of the 5C discharge process for various values of Q_0. As Q_0 increases, the airflow rate in the cooling channel increases, which increases the convective heat transfer coefficient between the air and the battery, reducing the cell temperatures. Thus, the values of T_{max} are reduced when Q_0 is increased. However, when Q_0 is large, the improvement of T_{max} is not obvious when increasing Q_0 further. Moreover, it can be observed from Figure 8 that the uniformity of the airflow rates among the cooling channels is worse when Q_0 is increased, leading to the larger temperature difference of the battery pack. Furthermore, when Q_0 increases, the power consumption to drive the airflow increases due to the increase of the drag force exerted by the walls. The power consumption for each situation is also listed in Table 6, which is calculated through:

$$W_p = (p_{in} - p_{out}) \cdot Q_0 \tag{12}$$

where p_{in} and p_{out} are the average pressures at the inlet cross-section and outlet cross-section, respectively. It can be seen from Table 6 that when Q_0 is increased from 0.012 m^3/s to 0.020 m^3/s, T_{max} is reduced by 2.1 K, but ΔT_{max} is increased by 2.0 K and W_p is increased by more than three-times. Therefore, increasing the inlet airflow rate can effectively reduce the maximum temperature, but it will increase the temperature difference of the battery pack and cost much additional power. It is not an effective way to improve the cooling performance of the BTMS through increasing the inlet airflow rate.

Table 6. Numerical results for various inlet airflow rates.

Q_0 (m^3/s)	T_{max} (K)	ΔT_{max} (K)	W_p (W)
0.005	329.5	4.4	0.0371
0.010	327.2	6.6	0.2295
0.012	326.5	7.3	0.3794
0.015	325.6	8.2	0.7094
0.020	324.3	9.3	1.6132

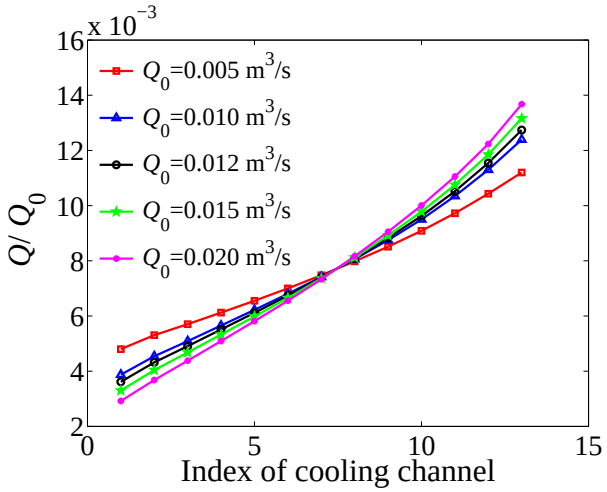

(**a**)

Figure 8. *Cont.*

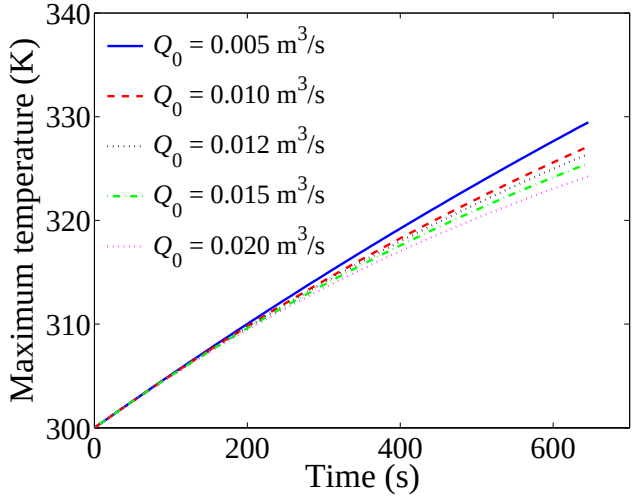

(**b**)

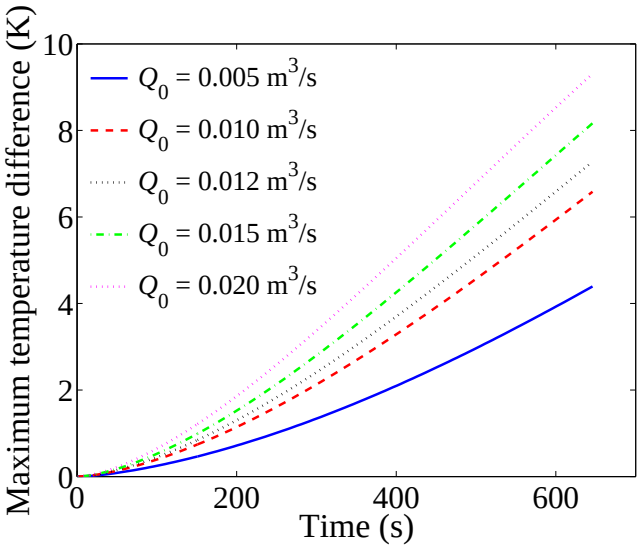

(**c**)

Figure 8. Comparison of results for various inlet airflow rates. (**a**) Flow rate in the cooling channel; (**b**) maximum temperature; (**c**) maximum temperature difference.

4.4. Influence of Cell Spacing

Consider various situations of the cell spacings (d_0) as 1 mm, 2 mm, 3 mm, 4 mm and 5 mm, and conduct the CFD calculation respectively. Figure 9 shows the comparison of the airflow rates in the cooling channels and the values of T_{max} and ΔT_{max} for various values of d_0. Table 7 summarizes the values of T_{max} and ΔT_{max} at the end of the 5C discharge process for various values of d_0. It can be seen from Figure 9 that as d_0 decreases, the uniformity of the airflow rates among the cooling channels is improved, which can help to reduce the temperature difference of the battery pack. Meanwhile, the velocities in the cooling channels increase as d_0 decreases, which will increase the convective heat transfer coefficient on the surface of the battery cells and reduce the cell temperatures. In the parallel air-cooled BTMS, the pressure drop of the airflow is caused by the drag force along the inlet duct and the outlet duct, the drag force along the cooling channels and the local pressure loss due to the swerve of the flow. The reduction of d_0 will remarkably increase the drag force along the cooling channel, making the drag force along the cooling channel dominate compared to other pressure losses. Therefore, the discrepancy of the airflow rates among the cooling channels is reduced

when d_0 is reduced. Meanwhile, the increase of the drag force along the cooling channel increases the power consumption to drive the airflow. It can be seen from Table 7 that compared to the system with $d_0 = 3$ mm, T_{max} and ΔT_{max} of the system with $d_0 = 1$ mm are reduced by 3.8 K and 2.8 K respectively, but W_p are increased by more than 10-times. Therefore, it is not an effective way to improve the cooling performance of the BTMS through reducing the cell spacing.

Table 7. Numerical results for various cell spacings.

d_0 (mm)	T_{max} (K)	ΔT_{max} (K)	W_p (W)
1	322.7	4.5	4.0044
2	324.0	4.7	0.7023
3	326.5	7.3	0.3794
4	329.5	11.0	0.3149
5	330.5	12.4	0.3056

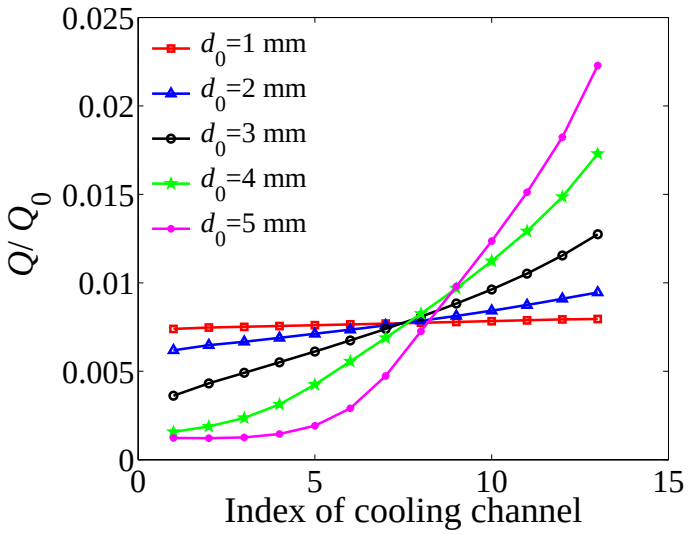

(**a**)

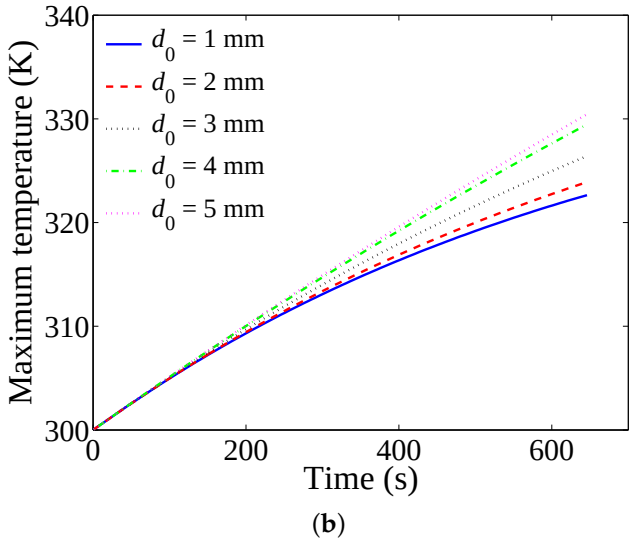

(**b**)

Figure 9. *Cont.*

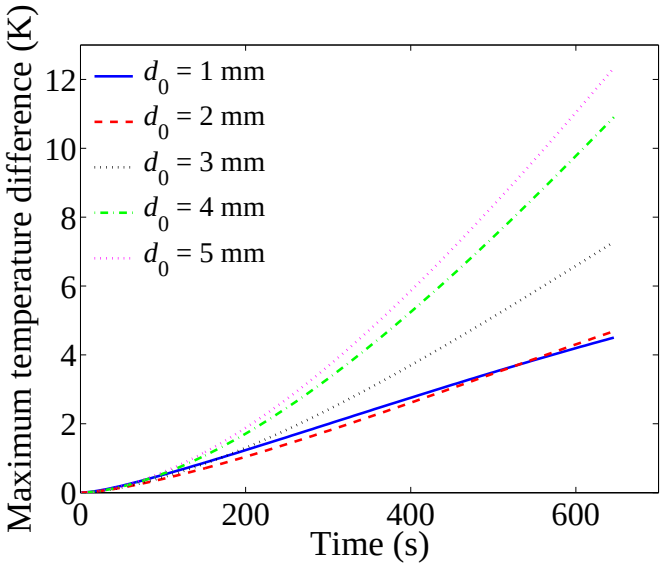

(**c**)

Figure 9. Comparison of the results for various cell spacings. (**a**) Flow rate in the cooling channel; (**b**) maximum temperature; (**c**) maximum temperature difference.

4.5. Influence of the Angles of the Divergence Plenum and Convergence Plenum

In this section, the angle of the divergence plenum (θ_1) and the angle of the convergence plenum (θ_2) are deduced from the plenum widths (w_1 and w_2), shown in Figure 2b. In the present study, w_1 and w_2 are values between 1 mm and 20 mm. Smaller w_1 and w_2 correspond to larger θ_1 and θ_2, respectively. The system with w_1 and w_2 both valued at 20 mm is treated as the original BTMS. Three situations are performed to investigate the influences of w_1 and w_2 on the system performance, shown as follows.

- Situation 1: Let $w_1 = 20$ mm, and consider the value of w_2 as 1 mm, 5 mm, 10 mm, 15 mm and 20 mm, respectively.
- Situation 2: Let $w_1 = w_2$, and consider the values as 1 mm, 5 mm, 10 mm, 15 mm and 20 mm, respectively.
- Situation 3: Let $w_2 = 20$ mm, and consider the value of w_1 as 1 mm, 5 mm, 10 mm, 15 mm and 20 mm, respectively.

For each combination of w_1 and w_2, CFD calculation is conducted, and the results are summarized in Table 8. For Situation 1, as w_2 decreases (θ_2 increases), T_{max}, ΔT_{max} and W_p all increase. That means, reducing w_2 makes the cooling performance of the BTMS worse and the relevant power consumption increases. For Situation 2, w_1 is equal to w_2. The results show that the values of w_1 and w_2 do not influence the T_{max} and ΔT_{max} of the system much. In this situation, the cooling performance of the system cannot be improved effectively through changing the angles of the divergence plenum and the convergence plenum. For Situation 3, it can be observed that T_{max} and ΔT_{max} are remarkably reduced when w_1 decreases while the power consumption of the system increases only a little. Compared to the original BTMS, T_{max} of the system with $w_1 = 1$ mm and $w_2 = 20$ mm is reduced by 2.5 K, and ΔT_{max} is reduced by 4.2 K. The improvement ratio of ΔT_{max} is 58%, while the power consumption is only increased by 23%.

Table 8. Numerical results for various angles of the divergence plenum and convergence plenum.

	w_1 (mm)	w_2 (mm)	T_{max} (K)	ΔT_{max} (K)	W_p (W)
Situation 1	20	1	329.1	11.0	0.4721
	20	5	328.0	9.5	0.4361
	20	10	327.2	8.4	0.4097
	20	15	326.8	7.8	0.3922
	20	20	326.5	7.3	0.3794
Situation 2	1	1	326.3	6.7	0.6296
	5	5	326.2	7.7	0.4991
	10	10	326.3	7.6	0.4379
	15	15	326.5	7.5	0.4032
	20	20	326.5	7.3	0.3794
Situation 3	1	20	324.0	3.1	0.4682
	5	20	325.0	5.8	0.4315
	10	20	325.7	6.7	0.4063
	15	20	326.2	7.1	0.3905
	20	20	326.5	7.3	0.3794

The cooling performance of the BTMS is strongly influenced by the homogenization of the flow rates among the cooling channels, which is determined by the homogenization of the pressure drops among the cooling channels. Figure 10 depicts the comparison of the numerical results of the typical BTMSs for the three situations. Figure 10a shows the cross-sectional average pressures at the beginning (denoted as "divergence") and at the end (denoted as "convergence") of each cooling channel. For the original BTMS, the cross-sectional areas along the inlet duct and the outlet duct are constants. Consider Point A and Point A′ in the inlet duct in Figure 11; along the inlet duct, the airflow speed gradually reduces towards the closed end as the air flows into the cooling channels, so the velocity at A (u_A) is larger than the one at A′ ($u_{A'}$). According to Bernoulli's equation, the pressure at A (p_A) is smaller than that at A′ ($p_{A'}$). Conversely, consider Point B and Point B′ in the outlet duct in Figure 11; along the outlet duct, the airflow speed gradually increases towards the outlet as the air flow converges into the outlet duct, so the velocity at B (u_B) is smaller than the one at B′ ($u_{B'}$). According to Bernoulli's equation, the pressure at B (p_B) is larger than that at B′ ($p_{B'}$). Therefore, $(p_A - p_B) < (p_{A'} - p_{B'})$. The pressure drop of the cooling channel near the outlet is much larger than that near the inlet for the original system, which can be seen in Figure 10b. The large discrepancy of the pressure drops among the cooling channels leads to nonuniformity of the airflow rates among the cooling channels and a large temperature difference for the battery pack. For Situation 1, when w_2 decreases, the pressures at Points A, A′, B and B′ are all increased, while the one at Point B is increased most significantly. Thus, the discrepancy between $(p_A - p_B)$ and $(p_{A'} - p_{B'})$ is enlarged. The uniformity of the airflow among the cooling channels and the cell temperature for the situation with w_2 decreasing is worse than that of the original system. Conversely, for Situation 3, the cross-sectional areas near the closed end of the inlet duct are reduced, causing $u_{A'}$ to be increased and $p_{A'}$ to be reduced. Meanwhile, the pressures along the outlet duct only change a little. Reducing w_1 will decrease the value of $(p_{A'} - p_{B'})$ and reduce the discrepancy of the pressure drops among the cooling channels, which can be observed in Figure 10b. Therefore, reducing w_1 when fixing w_2 can effectively reduce T_{max} and ΔT_{max} of the BTMS through arranging the pressure drop distribution among the cooling channels.

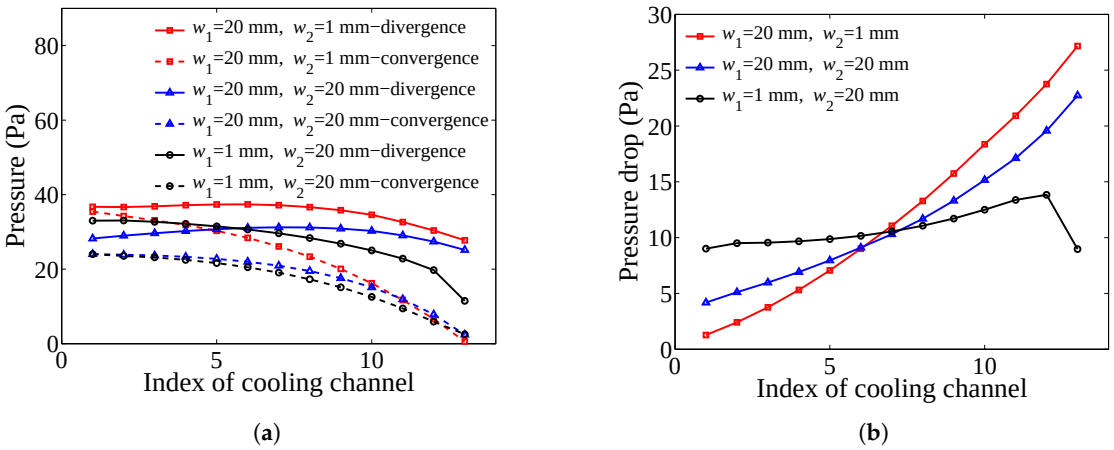

Figure 10. Comparison of numerical results for various angles of the plenums. (**a**) Pressure; (**b**) pressure drop.

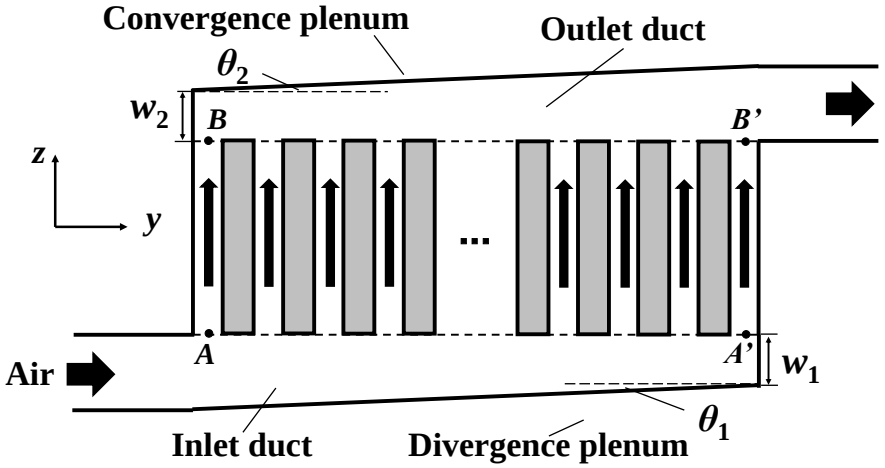

Figure 11. Schematic of the characteristic points in the air-cooled BTMS.

4.6. Optimization of Plenum Widths

In this section, an optimization strategy is used to optimize the plenum widths (w_1 and w_2). First, the value of w_2 is fixed, and the value of w_1 is optimized. Then, the value of w_1 is fixed and the value of w_2 is optimized. Take the optimization of w_1 as an example, the detailed steps of the optimization strategy are shown as follows.

1. Set w_2 as the fixed value and set the initial range of w_1 as $[w_{11}, w_{12}]$. Calculate the middle point of the range $[w_{11}, w_{12}]$ as $w_{13} = (w_{11} + w_{12})/2$.
2. Let w_1 equal w_{11}, w_{12} and w_{13}, respectively. Evaluate the values of $\Delta T_{\max}$ of these three BTMSs using the CFD calculation, respectively, denoting them as $\Delta T_{\max,1}$, $\Delta T_{\max,2}$ and $\Delta T_{\max,3}$.

   If $\Delta T_{\max,1} < \Delta T_{\max,3}$,

   let $w_{11} = w_{11}, w_{12} = w_{13}, w_{13} = (w_{11} + w_{12})/2$, then return to Step 2 and continue the process.

   else if $\Delta T_{\max,2} < \Delta T_{\max,3}$,

   let $w_{11} = w_{13}, w_{12} = w_{12}, w_{13} = (w_{11} + w_{12})/2$, then return to Step 2 and continue the process.

   else

   go to Step 3.

3. The range for w_1 is reduced through using the following strategy. Let $w_{14} = (w_{11} + w_{13})/2$ and $w_{15} = (w_{13} + w_{12})/2$. Evaluate the values of $\Delta T_{\max}$ of the two BTMSs with $w_1 = w_{14}$ and $w_1 = w_{15}$ using CFD calculation, respectively, denoting them as $\Delta T_{\max,4}$ and $\Delta T_{\max,5}$.

   If $\Delta T_{\max,4} < \Delta T_{\max,3}$,

   let $w_{11} = w_{11}, w_{12} = W_{13}, w_{13} = w_{14}, \Delta T_{\max,1} = \Delta T_{\max,1}, \Delta T_{\max,2} = \Delta T_{\max,3}, \Delta T_{\max,3} = \Delta T_{\max,4}$.

   else if $\Delta T_{\max,5} < \Delta T_{\max,3}$,

   let $w_{11} = w_{13}, w_{12} = w_{12}, w_{13} = w_{15}, \Delta T_{\max,1} = \Delta T_{\max,3}, \Delta T_{\max,2} = \Delta T_{\max,2}, \Delta T_{\max,3} = \Delta T_{\max,5}$.

   else

   let $w_{11} = w_{14}, w_{12} = w_{15}, w_{13} = w_{13}, \Delta T_{\max,1} = \Delta T_{\max,4}, \Delta T_{\max,2} = \Delta T_{\max,5}, \Delta T_{\max,3} = \Delta T_{\max,3}$.
4. If $(w_{13} - w_{11})$ and $(w_{12} - w_{13})$ are both smaller than a specified threshold, the optimization process is stopped; otherwise, return to Step 3, and continue the process.

When the process is stopped, the optimal value of w_1 is $w_{1,\text{opt}} = w_{13}$ and the relevant maximum temperature difference of the battery pack is $\Delta T_{\max,3}$. The value of w_2 when w_1 is fixed can also be optimized using the same strategy.

In the present study, the ranges of w_1 and w_2 are both set as [1.0 mm, 20.0 mm]. The threshold to stop the process is set as 0.1 mm. Considering the numerical results in Table 8, let $w_2 = 20.0$ mm and set the initial range of w_1 as [1.0 mm, 5.0 mm]. The detailed processes for the optimization of w_1 are listed in Table 9. Note that $\Delta T_{\max}$ increases as w_1 increases, and the final optimal value of w_1 is $w_{1,\text{opt}} = 1.0$ mm. Then, considering the numerical results in Table 8, let $w_1 = 1.0$ mm, and set the initial range of w_2 as [15.0 mm, 20.0 mm]. The detailed processes for the optimization of w_2 are listed in Table 10. Note that $\Delta T_{\max}$ decreases as w_2 increases, and the final optimal value of w_2 is $w_{2,\text{opt}} = 20.0$ mm. Therefore, the final optimal values of the plenum widths are $w_{1,\text{opt}} = 1.0$ mm and $w_{2,\text{opt}} = 20.0$ mm.

Table 9. The process of the optimization of w_1 ($w_2 = 20.0$ mm).

Step	w_{11}		w_{14}		w_{13}		w_{15}		w_{12}	
	w_1 (mm)	$\Delta T_{\max}$ (K)	w_1 (mm)	$\Delta T_{\max}$ (K)	w_1 (mm)	$\Delta T_{\max}$ (K)	w_1 (mm)	$\Delta T_{\max}$ (K)	w_1 (mm)	$\Delta T_{\max}$ (K)
1	1.00	3.08	-	-	3.00	5.10	-	-	5.00	5.80
2	1.00	3.08	-	-	2.00	4.43	-	-	3.00	5.10
3	1.00	3.08	-	-	1.50	3.92	-	-	2.00	4.43
4	1.00	3.08	-	-	1.25	3.61	-	-	1.50	3.92
5	1.00	3.08	-	-	1.13	3.32	-	-	1.25	3.61
6	1.00	3.08	-	-	1.06	3.21	-	-	1.13	3.32

Table 10. The process of the optimization of w_2 (w_1 = 1.0 mm).

Step	w_{11}		w_{14}		w_{13}		w_{15}		w_{12}	
	w_1 (mm)	ΔT_{max} (K)	w_1 (mm)	ΔT_{max} (K)	w_1 (mm)	ΔT_{max} (K)	w_1 (mm)	ΔT_{max} (K)	w_1 (mm)	ΔT_{max} (K)
1	15.00	3.45	-	-	17.50	3.25	-	-	20.00	3.08
2	17.50	3.25	-	-	18.75	3.16	-	-	20.00	3.08
3	18.75	3.16	-	-	19.38	3.12	-	-	20.00	3.08
4	19.38	3.12	-	-	19.69	3.10	-	-	20.00	3.08
5	19.69	3.10	-	-	19.84	3.09	-	-	20.00	3.08
6	19.84	3.09	-	-	19.92	3.09	-	-	20.00	3.08

4.7. Performance with Fixed Power Consumption

The system with the optimal values of w_1 at 1 mm and w_2 at 20 mm is named the optimized BTMS in this section. It can be seen from Table 8 that the optimized BTMS requires more power consumption than the original system. The increased power consumption will increase the cost of the BTMS, which is not expected in the application. In order to evaluate the cooling performance of the optimized BTMS under the same power consumption, the inlet airflow rate of the optimized system is decreased to match the power consumption of the original BTMS. When the inlet airflow rate is set as 0.01112 m^3/s, the relevant power consumption is 0.3794 W, the same as the one of the original system. The final inlet flow rate of the optimized BTMS is only reduced by 7% compared to the original inlet flow rate. Though the inlet flow rate is reduced, the maximum temperature and the maximum temperature difference of the battery pack for the optimal BTMS are still remarkably lower than the ones of the original BTMS, which can be observed from Figure 12. T_{max} and ΔT_{max} of the optimized BTMS with the fixed power consumption are respectively 324.4 K and 3.0 K, which are respectively 2.1 K and 4.3 K lower than the ones of the original system. Furthermore, the reduction of the angle of the divergence plenum will not increase the total volume of the BTMS. In summary, choosing appropriate values of the plenum widths (the angles of the plenums) can help to homogenize the pressure drops among the cooling channels and to improve the cooling performance of the BTMS remarkably.

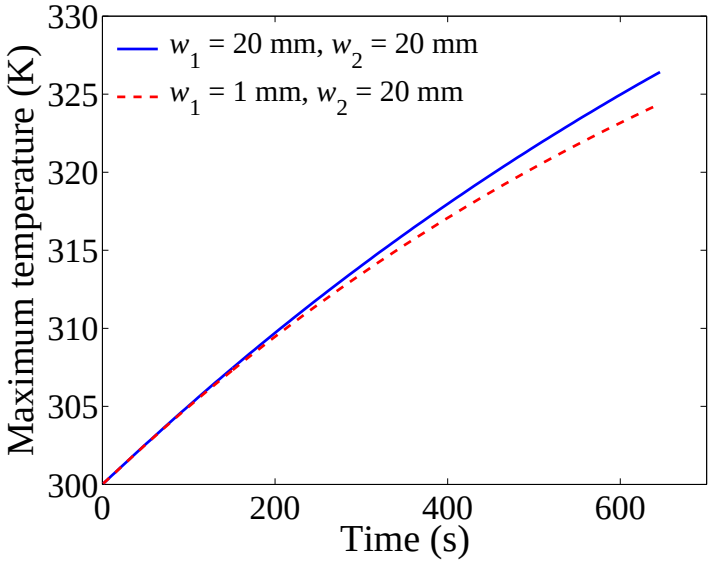

(**a**)

Figure 12. *Cont.*

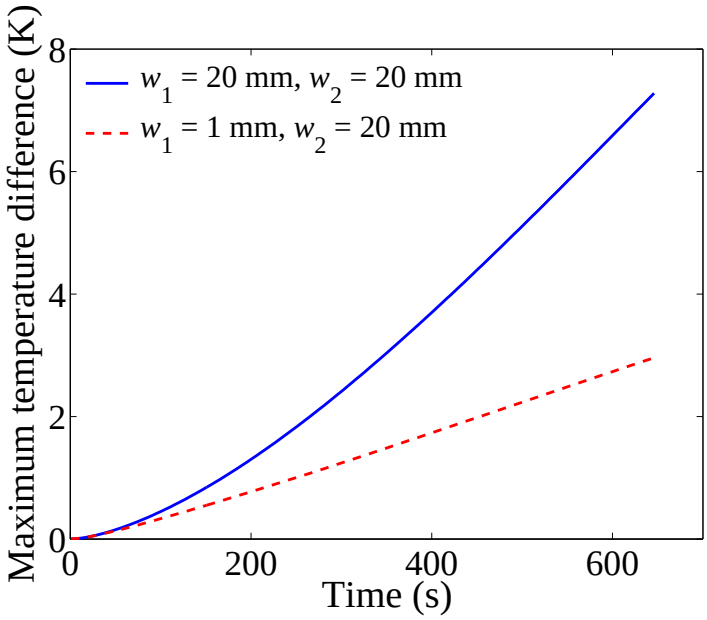

(**b**)

Figure 12. Comparison of the maximum temperature and the maximum temperature difference of the battery pack with time with fixed power consumption. (**a**) Maximum temperature; (**b**) maximum temperature difference.

5. Conclusions

In the present study, the cooling performance of the parallel air-cooled BTMS is improved through using appropriate system parameters. The CFD method is introduced to evaluate the performance of the system. Typical numerical cases are employed to explore the influences of the operation parameters and the structure parameters on the cooling performance of the BTMS. Then, an optimization strategy is proposed to obtain the optimal parameters of the system.

1. The temperature rise and the temperature difference of the battery pack increase as the discharge rate increases, but the discharge rate cannot be controlled effectively.
2. Reducing the inlet air temperature can reduce the absolute temperature of the battery pack, but cannot effectively reduce the temperature rise and the temperature difference of the system.
3. As the inlet airflow rate increases, the maximum temperature of the battery pack is reduced, but the temperature difference of the battery pack and the power consumption to maintain the flow rate are both increased.
4. As the cell spacings decrease, the temperature and the temperature difference of the battery pack are both reduced effectively. However, the decrease of the cell spacing increases the power consumption of the system significantly.
5. The angles of the plenums remarkably influence the performance of the BTMS. The maximum temperature and the maximum temperature difference of the battery pack can be reduced effectively through optimizing the angles of the plenums, without increasing the total volume and the power consumption of the BTMS.

Through the analysis above, it can be concluded that the performance of the BTMS can be improved through arranging the flow pattern of the system, where changing the angles of the plenums is one of the most effective approaches. This approach can reduce the temperature and temperature difference of the battery pack when maintaining the power consumption and the volume of the BTMS, which is expected to be applied to design the structure of the BTMS.

Acknowledgments: This research is supported by the National Natural Science Foundation of China (Grant Nos. 51506056 and 51536003), the Fundamental Research Funds for the Central Universities (Grant No. 2017MS017) and the National Undergraduate Innovative Training Program (Grant No. 201710561094).

Author Contributions: Kai Chen and Shuangfeng Wang conceived of and designed the numerical study. Kai Chen performed the numerical calculation. Kai Chen, Zeyu Li, Yiming Chen and Shuming Long analyzed the data. Kai Chen wrote the paper. Mengxuan Song and Junsheng Hou checked the manuscript.

Conflicts of Interest: The authors declare no conflict of interest. The founding sponsors had no role in the design of the study; in the collection, analyses or interpretation of data; in the writing of the manuscript; nor in the decision to publish the results.

Nomenclature

C_1, C_2	parameters of the $k \sim \varepsilon$ turbulence model, 1
C_μ	parameter of the $k \sim \varepsilon$ turbulence model, 1
$c_{p,\mathrm{air}}$	heat capacities of the air, $\mathrm{J}/(\mathrm{kg} \cdot \mathrm{K})$
$c_{p,\mathrm{b}}$	heat capacities of the battery cell, $\mathrm{J}/(\mathrm{kg} \cdot \mathrm{K})$
d_0	cell spacing among the battery cells, m
$l_\mathrm{b}, w_\mathrm{b}, h_\mathrm{b}$	length, width and height of the battery cell, m
I	discharge current of the battery cell, A
k	turbulent kinetic energy, $\mathrm{m}^2/\mathrm{s}^2$
M	number of the rows for the battery pack, 1
N	number of the columns for the battery pack, 1
p	Reynolds-averaged pressure, Pa
Q_0	inlet airflow rate, m^3/s
R	the equivalent resistance of the battery cell, Ω
T_0	temperature of the inlet airflow, K
T_air	temperature of the air, K
T_b	temperature of the battery cell, K
T_max	maximum temperature of the battery pack, K
ΔT_max	maximum temperature difference of the battery pack, K
u_i, u_j	the i-th and the j-th Reynolds-averaged velocity components, m/s
V_cell	volume of the battery cell, m^3
w_1	width of the divergence plenum, m
w_2	width of the convergence plenum, m
w_in	inlet width, m
w_out	outlet width, m
W_p	power consumption of the BTMS, W
x, y, z	coordinates of the domain, m

Greek Symbols

λ_air	thermal conductivity of the air, $\mathrm{W}/(\mathrm{m} \cdot \mathrm{K})$
λ_b	thermal conductivity of the battery cell, $\mathrm{W}/(\mathrm{m} \cdot \mathrm{K})$
μ	the molecular dynamic viscosity coefficient of the air, $\mathrm{kg}/(\mathrm{m} \cdot \mathrm{s})$
μ_t	the turbulent dynamic viscosity coefficient, $\mathrm{kg}/(\mathrm{m} \cdot \mathrm{s})$
ϕ_b	heat generation rate of the battery cell, W/m^3
ρ	density of the air, kg/m^3
ρ_b	density of the battery cell, kg/m^3
σ_ε	parameter of the $k \sim \varepsilon$ turbulence model in the ε equation, 1
σ_k	parameter of the $k \sim \varepsilon$ turbulence model in the k equation, 1
σ_T	parameter of the $k \sim \varepsilon$ turbulence model in the temperature equation, 1
θ_1	angle of the divergence plenum, degree
θ_2	angle of the convergence plenum, degree
ε	turbulent kinetic energy dissipation, $\mathrm{m}^2/\mathrm{s}^3$

Subscripts

b	battery cell
in	inlet cross-section
max	maximum
out	outlet cross-section

References

1. Li, X.; He, F.; Ma, L. Thermal management of cylindrical batteries investigated using wind tunnel testing and computational fluid dynamics simulation. *J. Power Sources* **2013**, *238*, 395–402.
2. Xing, Y.; He, W.; Pecht, M.; Tsui, K.L. State of charge estimation of lithium-ion batteries using the open-circuit voltage at various ambient temperatures. *Appl. Energy* **2014**, *113*, 106–115.
3. He, F.; Li, X.; Ma, L. Combined experimental and numerical study of thermal management of battery module consisting of multiple Li-ion cells. *Int. J. Heat Mass Transf.* **2014**, *72*, 622–629.
4. Yu, K.; Yang, X.; Cheng, Y.; Li, C. Thermal analysis and two-directional air flow thermal management for lithium-ion battery pack. *J. Power Sources* **2014**, *270*, 193–200.
5. Mohammadian, S.K.; Zhang, Y. Thermal management optimization of an air-cooled Li-ion battery module using pin-fin heat sinks for hybrid electric vehicles. *J. Power Sources* **2015**, *273*, 431–439.
6. Jarrett, A.; Kim, I.Y. Design optimization of electric vehicle battery cooling plates for thermal performance. *J. Power Sources* **2001**, *196*, 10359–10368.
7. Smith, J.; Hinterberger, M.; Hable, P.; Koehler, J. Simulative method for determining the optimal operating conditions for a cooling plate for lithium-ion battery cell modules. *J. Power Sources* **2014**, *267*, 784–792.
8. Qian, Z.; Li, Y.; Rao, Z. Thermal performance of lithium-ion battery thermal management system by using mini-channel cooling. *Energy Convers. Manag.* **2016**, *126*, 622–631.
9. Sabbah, R.; Kizilel, R.; Selman, J.R.; Al-Hallaj, S. Active (air-cooled) vs. passive (phase change material) thermal management of high power lithium-ion packs: Limitation of temperature rise and uniformity of temperature distribution. *J. Power Sources* **2008**, *182*, 630–638.
10. Rao, Z.; Wang, Q.; Huang, C. Investigation of the thermal performance of phase change material/mini-channel coupled battery thermal management system. *Appl. Energy* **2016**, *164*, 659–669.
11. Alipanah, M.; Li, X. Numerical studies of lithium-ion battery thermal management systems using phase change materials and metal foams. *Int. J. Heat Mass Transf.* **2016**, *102*, 1159–1168.
12. Wilke, S.; Schweitzer, B.; Khateeb, S.; Al-Hallaj, S. Preventing thermal runaway propagation in lithium ion battery packs using a phase change composite material: An experimental study. *J. Power Sources* **2017**, *340*, 51–59.
13. Yi, J.; Koo, B.; Shin, C. Three-Dimensional Modeling of the Thermal Behavior of a Lithium-Ion Battery Module for Hybrid Electric Vehicle Applications. *Energies* **2014**, *7*, 7586–7601.
14. Cho, G.Y.; Choi, J.W.; Park, J.H.; Cha, S.W. Transient modeling and validation of lithium ion battery pack with air cooled thermal management system for electric vehicles. *Int. J. Automot. Technol.* **2014**, *15*, 795–803.
15. Fan, L.; Khodadadi, J.M.; Pesaran, A.A. A parametric study on thermal management of an air-cooled lithium-ion battery module for plug-in hybrid electric vehicles. *J. Power Sources* **2013**, *238*, 301–312.
16. Liu, Z.; Wang, Y.; Zhang, J.; Liu, Z. Shortcut computation for the thermal management of a large air-cooled battery pack. *Appl. Therm. Eng.* **2014**, *66*, 445–452.
17. He, H.; Jia, H.; Huo, W.; Sun, F. Field Synergy Analysis and Optimization of the Thermal Behavior of Lithium Ion Battery Packs. *Energies* **2017**, *10*, 811.
18. Pesaran, A.A. Battery thermal models for hybrid vehicle simulations. *J. Power Sources* **2002**, *110*, 377–382.
19. Mahamud, R.; Park, C. Reciprocating air flow for Li-ion battery thermal management to improve temperature uniformity. *J. Power Sources* **2011**, *196*, 5685–5696.
20. Wang, T.; Tseng, K.J.; Zhao, J.; Wei, Z. Thermal investigation of lithium-ion battery module with different cell arrangement structures and forced air-cooling strategies. *Appl. Energy* **2014**, *134*, 229–238.
21. Yong, S.C.; Mo, K.D. Prediction of thermal behaviors of an air-cooled lithium-ion battery system for hybrid electric vehicles. *J. Power Sources* **2014**, *270*, 273–280.

22. Park, H. A design of air flow configuration for cooling lithium ion battery in hybrid electric vehicles. *J. Power Sources* **2013**, *239*, 30–36.
23. Sun, H.; Dixon, R. Development of cooling strategy for an air cooled lithium-ion battery pack. *J. Power Sources* **2014**, *272*, 404–414.
24. Chen, K.; Wang, S.; Song, M.; Chen, L. Structure optimization of parallel air-cooled battery thermal management system. *Int. J. Heat Mass Transf.* **2017**, *111*, 943–952.
25. Shahid, S.; Agelin-Chaab, M. Analysis of Cooling Effectiveness and Temperature Uniformity in a Battery Pack for Cylindrical Batteries. *Energies* **2017**, *10*, 1157.
26. Xu, X.M.; He, R. Research on the heat dissipation performance of battery pack based on forced air cooling. *J. Power Sources* **2013**, *240*, 33–41.
27. Xu, X.M.; He, R. Review on the heat dissipation performance of battery pack with different structures and operation conditions. *Renew. Sustain. Energy Rev.* **2014**, *29*, 301–315.
28. Panchal, S.; Khasow, R.; Dincer, I.; Agelin-Chaab, M.; Fraser, R.; Fowler, M. Thermal design and simulation of mini-channel cold plate for water cooled large sized prismatic lithium-ion battery. *Appl. Therm. Eng.* **2017**, *22*, 80–90.
29. Panchal, S.; Khasow, R.; Dincer, I.; Agelin-Chaab, M.; Fraser, R.; Fowler, M. Numerical modeling and experimental investigation of a prismatic battery subjected towater cooling. *Numer. Heat Transf. Part A Appl.* **2017**, *71*, 626–637.
30. Chen, K.; Wang, S.; Song, M.; Chen, L. Configuration optimization of battery pack in parallel air-cooled battery thermal management system using an optimization strategy. *Appl. Therm. Eng.* **2017**, *123*, 177–186.
31. Wu, W. The Experimental and Simulation Research of Power Batteries Thermal Management Based on PCM. Master's Thesis, Guangdong University of Technology, Guangzhou, China, 2015.